Engineering Fracture Mechanics 138 (2015) 19–32

Contents lists available at ScienceDirect

Engineering Fracture Mechanics

journal homepage: www.elsevier.com/locate/engfracmech

A porous-based discontinuous model for ductile fracture in metals

Diego Said Schicchi [a,*], Antonio Caggiano [b]

[a] Stiftung Institut für Werkstofftechnik (IWT), Bremen, Germany
[b] CONICET and University of Buenos Aires, Argentina

ARTICLE INFO

Article history:
Received 20 December 2014
Received in revised form 24 February 2015
Accepted 2 March 2015
Available online 12 March 2015

Keywords:
Ductile fracture
Porous plasticity
Interface model
Discontinuous FEM

ABSTRACT

A discontinuous model aimed at modeling ductile fracture for metals is presented. The effect of microvoid nucleation, growth and coalescence on the inelastic response of structural metals is modeled through a suitable interface proposal for cracking analysis. The discontinuos proposal is completely conceived within the general framework of fracture mechanics and porous plasticity concepts. The porosity affects the strength parameters and softening rules defining the failure initiation and post-cracking response of the interface. To demonstrate the soundness and capability of the proposed formulation, a comparative study against numerical simulations obtainable from a classical well-known continuous approach for capturing ductile fracture, based on finite element analysis, is presented.

1. Introduction

Ductile fracture in metals usually follows a multi-step inelastic process involving several concurrent mechanisms, which, at microscopic level, can be subdivided into (a) nucleation of microscopic voids (mostly at second phase particles and inclusions), (b) growth of fine microscopic voids due to localized inelastic deformation and eventual coalescence, (c) localization of plastic flow (the crack initiation) and (d) final failure and crack growing [1,2].

Void nucleation, growth and coalescence and the subsequent crack initiation deal with two distinct mechanisms of ductile fracture [3]: (i) the first mechanism is represented by a crack growth initiation as a consequence of a single void and interacting with the crack tip along the fracture front, while (ii) the second failure considers the simultaneous growth and interaction of multiple voids on the plane ahead of the crack tip.

Moreover, failure under intense shearing at close to zero hydrostatic stress (the mean stress is zero or even negative) is widely observed for ductile metallic materials [4]. Experimental studies [5] and numerical formulations by Barsoum and Faleskog [6,7] aimed at investigating ductile failure under such conditions. Furthermore, the progressive reduction of material ductility with increasing triaxial stress was investigated by Bonora et al. [8] and Benzerga et al. [9], while the temperature effect on the ductile fracture of metal was considered in several works [10,11].

Ductile failure mechanisms and simulations of crack growth in metals are classically analyzed through several of constitutive formulations which mainly represent modified versions or extensions of the model originally developed by Gurson [12]. His study dealt with the growth of a single spherical void which produces the development of ductile fracture.

* Corresponding author. Tel.: +49 (0)421 218 51326.
E-mail addresses: schicchi@iwt.uni-bremen.de (D. Said Schicchi), acaggiano@fi.uba.ar (A. Caggiano).

http://dx.doi.org/10.1016/j.engfracmech.2015.03.008
0013-7944/

Nomenclature

A	nucleation parameter of the continuous model
A_{IE}	nucleation parameter of the interface model
$\mathbf{C}$	elastic stiffness matrix
$\mathbf{C}^{ep}$	tangential interface stiffness matrix for elasto-plastic degradation
E	Young's modulus
f	void volume fraction (porosity)
f_C	void volume fraction value at the beginning of the coalescence
f_F	void volume fraction value corresponding to a total failure
f_0	initial void volume fraction
f^*	modified void volume fraction function
f_{gro}	void volume fraction due to growth of existing voids
f_{nuc}	void volume fraction due to nucleation of new voids
f_N	volume fraction of the nucleated voids for the normal distribution
G	shear modulus
H^α	set of scalar state variables
$\bar{H}$	softening parameter
k_N	normal elastic stiffness
k_T	tangential elastic stiffness
l	thickness of the joint
$\mathbf{n}$	vector outlining the direction of the interface fracture displacements
N	hardening exponent of the power hardening law
q_β	internal parameters of the yield function
s_N	standard deviation value for the nucleation normal distribution of the GTN model
$s_{N_{IE}}$	standard deviation value for the nucleation normal distribution of the interface model
$\mathbf{t}$	interface contact stress vector
$\mathbf{u}$	relative interface displacement vector
$\mathbf{u}^{el}$	elastic part of the relative interface displacement vector
$\mathbf{u}^{p}$	plastic part of the relative interface displacement vector
u	relative interface normal displacement
$\bar{u}$	equivalent plastic interface displacement
$\dot{\bar{u}}$	equivalent plastic interface displacement rate
u_0	elastic limit relative displacement for the interface hardening law
u_N	model parameter to be calibrated for the nucleation description
v	relative interface transversal displacement
$\bar{\varepsilon}$	equivalent plastic strain
ε_N	mean strain value for the nucleation normal distribution
ε_0	elastic strain limit
ϕ	yield function equation
$\dot{\lambda}$	non-negative plastic multiplier
ν	Poisson's coefficient
θ	mixed mode load angle
σ	normal interface contact stress
σ_0	yield stress of the interface fully dense matrix material
σ_e	von Mises stress
σ_m	hydrostatic pressure
σ_y	initial matrix yield strength
$\bar{\sigma}$	yield stress of the continuous fully dense matrix material
τ	shear interface contact stress

Enakoutsa [13] developed a nonlocal methodology to delocalize the damage in Gurson model for porous ductile materials. An original way to account for the surface/interface stresses effect at micro-scale, between the nano-inclusion and the surrounding matrix, was extended for the classical Gurson model for ductile porous media by Dormieux and Kondo [14]. A modified Gurson model was also developed by Jackiewicz [15] for the simulation of damage growth and ductile fracture under low, medium and high triaxial stresses. A phenomenological modification to the Gurson model that incorporates damage accumulation under shearing was proposed by Nahshon and Xue [16]. Furthermore, Nahshon and Hutchinson [17]

proposed an extension of the Gurson formulation which models damage growth under low triaxiality straining for shear-dominated states. Further extensions of the original Gurson formulation are available in literature [18–20].

This work presents a zero-thickness interface model for ductile fracture. The formulation is based on the flow theory of plasticity and porous-based concepts to control the energy release during cracking processes in Mode I, II and mixed. This model represents a new extension of the continuous formulation classically known as the modified Gurson model or Gurson–Tvergaard–Needleman (GTN) model [21].

After the above introduction, the paper is organized as follows. Section 2 reports the general formulation and basic assumptions of the elasto-plastic interface model. Section 3 figures out the failure criterion outlining the crack initiation of the interface model while Section 4 deals with the calculation of the tangent constitutive tensor. Then, the classical continuous formulation and the adopted techniques to create a link between this and the corresponding discontinuous approach are discussed in Section 5. Finally, the study for capturing ductile fracture by comparing these two approaches is presented and discussed in Section 6.

It is worth mentioning that the interface model proposed in this paper can be employed in microscopic analyses aimed at simulating failure processes developed at the inclusion-surrounding matrix interfaces [22]. A micro-mechanical approach (and the consequent possibility of modeling the behavior of ductile fracture in metals starting from both their components and the interactions among them) represents the key contribution of the proposed model.

Under micro and mesoscale levels of observation, the increasing damage of ductile materials gives rise to the development of discontinuous cracks, representing first order displacement discontinuities which, e.g. in some steels, can evolve at interfaces of second phase particles and inclusions of the material under consideration. Therefore, the fixed crack approach, based on the proposed porosity-based interface model, represents the most appropriate and direct procedure to model the mechanical response and the displacement jumps in the aforementioned discontinuities. A fundamental advantage of this approach, based on zero-thickness interfaces, is the related objectivity of the FE predictions of localized failure processes regarding mesh size and orientation, provided when a sufficient mesh density is considered. Furthermore, Finite Element Analyses (FEA) based on zero thickness interfaces are characterized by the inexistence of element locking which constitutes a relevant shortcoming of classical continuous-based thin-layer FEA.

2. The porous-based interface model

The constitutive zero-thickness Interface Element (IE) formulation is inspired on the modified Gurson model [12,21,23–25] which is typically employed to model ductile damage. A brief description of the continuous approach is summarized in Section 5.1.

The proposed model is based on the following rate constitutive equations [26,27]

$$\dot{\mathbf{u}} = \dot{\mathbf{u}}^{el} + \dot{\mathbf{u}}^{p} \tag{1a}$$

$$\dot{\mathbf{u}}^{el} = \mathbf{C}^{-1} \cdot \dot{\mathbf{t}} \tag{1b}$$

$$\dot{\mathbf{t}} = \mathbf{C} \cdot (\dot{\mathbf{u}} - \dot{\mathbf{u}}^{p}) \tag{1c}$$

being

$$\dot{\mathbf{u}} = [\dot{u}, \dot{v}]^{T} \tag{2}$$

the rate of the relative interface displacement vector, decomposed into the elastic part, $\dot{\mathbf{u}}^{el}$, and the plastic one, $\dot{\mathbf{u}}^{p}$; with $\dot{u}$ and $\dot{v}$ the relative displacements rate in the normal and tangential direction, respectively; whereas $\dot{\mathbf{t}} = [\dot{\sigma}, \dot{\tau}]^{T}$ is the vector of the incremental contact stress defined in the interface plane, being σ and τ the normal and shear components, respectively.

$\mathbf{C}$ defines the elastic stiffness matrix

$$\mathbf{C} = \begin{pmatrix} k_N & 0 \\ 0 & k_T \end{pmatrix} \tag{3}$$

with k_N and k_T representing the normal and tangential elastic contact stiffnesses.

The vector of the plastic displacement rate, $\dot{\mathbf{u}}^{p}$, is defined according to the following associated flow rule

$$\dot{\mathbf{u}}^{p} = \dot{\lambda}\mathbf{n} = [\dot{u}^{p}, \dot{v}^{p}]^{T}. \tag{4}$$

The non-negative plastic multiplier, $\dot{\lambda}$, is derived starting from the classical Kuhn–Tucker loading/unloading (Eq. (5a)) and consistency (Eq. (5b)) conditions

$$\dot{\lambda} \geqslant 0, \ \phi \leqslant 0, \ \dot{\lambda}\phi = 0 \tag{5a}$$

$$\dot{\lambda}\dot{\phi} = 0 \tag{5b}$$

being $\phi = \phi(\sigma, \tau, H^{\alpha})$ the yield function of the model, with H^{α} ($\alpha = 1, 2, \ldots, n$) a set of scalar state variables. The $\mathbf{n}$ vector, outlining the direction of the interface fracture displacements, can be calculated as follows

$$\mathbf{n} = \frac{\partial \phi}{\partial \mathbf{t}} = \left[\frac{\partial \phi}{\partial \sigma}, \frac{\partial \phi}{\partial \tau}\right]^T. \tag{6}$$

3. Loading and failure criteria

The yield function for the porous interface model is defined by means of the following criterion (outlining the surface represented in Fig. 1)

$$\phi(\mathbf{t}, \bar{u}, f) = q_4\left(\frac{\tau}{\sigma_0}\right)^2 + 2q_1 f^* \cosh\left(\frac{3}{2}q_2\frac{\sigma}{\sigma_0}\right) - \left(1 + q_3 f^{*2}\right) \tag{7}$$

being q_β ($\beta = 1,2,3,4$) internal parameters to be calibrated, $\sigma_0 = \sigma_0(\bar{u})$ the yield stress, which refers to the so called *matrix material* (dealing with the material without voids), depending on the equivalent plastic interface displacement $\bar{u}$. Then, $f^* = f^*(f)$ is the modified porosity function which simulates the accelerated loss of strength due to the coalescence phenomenon [21]

$$f^* = \begin{cases} f & \text{if} \quad f \leqslant f_C \\ f_C + \frac{\frac{1}{q_1} - f_C}{f_F - f_C}(f - f_C) & \text{if} \quad f_C < f < f_F \end{cases} \tag{8}$$

where f_C is the value for the porosity at the beginning of the coalescence and f_F the value at which the total fracture is reached. It is worth noting that a fully dense material implies that $f = f^* = 0$ with no softening whatsoever. On the opposite side, in case of failure, where $f = f_F$, the limit value of the modified porosity corresponds to $f^* = 1/q_1$.

The function f deals with the nucleation of new voids as well as the growth of the existing ones [21]. Therefore, the evolution of the void volume fraction is governed as follows

$$\dot{f} = \dot{f}_{gro} + \dot{f}_{nuc} \tag{9}$$

where the growth of the existing voids is a function of the plastic uplift rate, $\dot{u}^p$,

$$\dot{f}_{gro} = (1 - f)\frac{\dot{u}^p}{l} \tag{10}$$

being l a length which represents the thickness of the joint layer.

The nucleation of new voids, developed only in case of tension, is given by the following expression

$$\dot{f}_{nuc} = A_{IE}\dot{\bar{u}} \tag{11}$$

with $\dot{\bar{u}}$ the rate of the interface equivalent plastic displacement. The expression of A_{IE} is described adopting a controlled nucleation following a normal distribution as follows

$$A_{IE} = \frac{f_N}{s_{N_{IE}}\sqrt{2\pi}} exp\left[-\frac{1}{2}\left(\frac{\bar{u} - u_N}{s_{N_{IE}}}\right)^2\right] \tag{12}$$

where f_N, $s_{N_{IE}}$ and u_N are model parameters to be calibrated, as highlighted in Section 6.1.

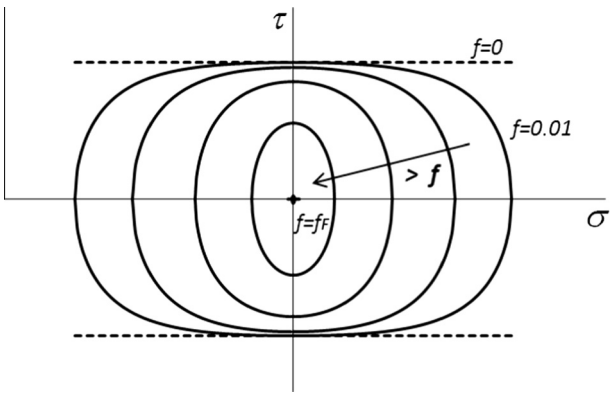

Fig. 1. Yield surface evolution depending on the porosity up to failure.

The rate of the equivalent interface plastic displacement is linked to the normal and tangential plastic displacement rates for the joint through the imposition of the equivalence between the rate of plastic work spent in the matrix material and the overall one as follows

$$(1-f)\sigma_0\dot{\bar{u}} = \mathbf{t}\cdot\dot{\mathbf{u}}^{\mathbf{p}} = \sigma\dot{u}^p + \tau\dot{v}^p \tag{13}$$

then, it can be derived the expression for $\dot{\bar{u}}$

$$\dot{\bar{u}} = \frac{\mathbf{t}\cdot\dot{\mathbf{u}}^p}{(1-f)\sigma_0} \tag{14}$$

and the total interface equivalent plastic displacement, $\bar{u}$, can be calculated by integrating the above equation during the fracture process.

Finally, depending on the total interface equivalent plastic displacement $\bar{u}$, the following hardening law is adopted

$$\sigma_0 = \sigma_y\left(1+\frac{\bar{u}}{u_0}\right)^N \tag{15}$$

where σ_y is the initial yield limit of matrix, N a hardening exponent and u_0 the elastic limit relative displacement.

4. Elasto-plastic constitutive equations

At the core of the nonlinear finite-element solver resides the tangent constitutive tensor which is calculated starting from the consistency condition of Eq. (5b) [28]. Particularly, for an inelastic load step with a positive plastic multiplier $\left(\dot{\lambda}>0\right)$ it follows that

$$\dot{\lambda}\dot{\phi} = 0 \quad \Rightarrow \quad \dot{\phi} = 0 \tag{16}$$

and consequently

$$\frac{\partial\phi}{\partial\mathbf{t}}\cdot\dot{\mathbf{t}} + \frac{\partial\phi}{\partial f}\dot{f} + \frac{\partial\phi}{\partial\bar{u}}\dot{\bar{u}} = 0. \tag{17}$$

4.1. Plastic multiplier

The classical expression for the incremental plastic multiplier is obtained by solving Eq. (17), replacing it into the constitutive Eq. (1c), accounting the evolution of porosity from Eq. (9) and the rate of the equivalent plastic displacement from Eq. (14).

After some algebra, the plastic multiplier in compact form becomes

$$\dot{\lambda} = \frac{\mathbf{n}\cdot\mathbf{C}}{\mathbf{n}\cdot\mathbf{C}\cdot\mathbf{n}+\bar{H}}\cdot\dot{\mathbf{u}} \tag{18}$$

where the softening parameter (namely $\bar{H}$) is represented by the following expression

$$\bar{H} = -\phi_{,f}\left((1-f)n_1 + A\frac{\mathbf{t}\cdot\mathbf{n}}{(1-f)\sigma_0}\right) - \left(\phi_{,\bar{u}}\frac{\mathbf{t}\cdot\mathbf{n}}{(1-f)\sigma_0}\right) \tag{19}$$

being $n_1 = \frac{\partial\phi}{\partial\sigma}$, $\phi_{,f} = \frac{\partial\phi}{\partial f}$ and $\phi_{,\bar{u}} = \frac{\partial\phi}{\partial\bar{u}}$.

4.2. Tangent stiffness operator

Consequently, the rate of normal and tangential interface stresses can be derived by the rate of interface displacements as

$$\dot{\mathbf{t}} = \mathbf{C}^{ep}\cdot\dot{\mathbf{u}}. \tag{20}$$

The plastic multiplier from Eq. (18) is replaced into the associated flow rule (Eq. (4)). These are then replaced into Eq. (1c) obtening, after some algebra, the following tangential interface stiffness for elasto-plastic degradation

$$\mathbf{C}^{ep} = \left(\mathbf{C} - \frac{\mathbf{C}\cdot\mathbf{n}\otimes\mathbf{n}\cdot\mathbf{C}}{\mathbf{n}\cdot\mathbf{C}\cdot\mathbf{n}+\bar{H}}\right). \tag{21}$$

4.3. Derivatives

All the derivatives needed from Eqs. (18)–(21) are reported below

$$\frac{\partial \phi}{\partial \sigma} = \frac{3f^* q_1 q_2 \sinh\left(\frac{3q_2\sigma}{2\sigma_0}\right)}{\sigma_0}; \tag{22}$$

$$\frac{\partial \phi}{\partial \tau} = \frac{2q_4\tau}{\sigma_0^2}; \tag{23}$$

$$\frac{\partial f^*}{\partial f} = \begin{cases} 1 & if \quad f \leqslant f_C \\ \frac{1}{\frac{q_1}{f_F - f_C}} & if \quad f_C < f < f_F \end{cases}; \tag{24}$$

$$\phi_{,f} = \frac{\partial \phi}{\partial f} = \frac{\partial \phi}{\partial f^*}\frac{\partial f^*}{\partial f} = \left[2q_1 \cosh\left(\frac{3q_2\sigma}{2\sigma_0}\right) - 2f^* q_3\right]\frac{\partial f^*}{\partial f}; \tag{25}$$

$$\phi_{,\bar{u}} = \frac{\partial \phi}{\partial \bar{u}} = \frac{\partial \phi}{\partial \sigma_0}\frac{\partial \sigma_0}{\partial \bar{u}} = -\frac{3f^* q_1 q_2 \sigma\sigma_0 \sinh\left(\frac{3q_2\sigma}{2\sigma_0}\right) + 2q_4\tau^2}{\sigma_0^3}\frac{\partial \sigma_0}{\partial \bar{u}}. \tag{26}$$

5. Continuous GTN model and homogenization against the interface proposal

The well-known *Porous metal plasticity model* available in Abaqus [29] is used at the continuous standpoint in this work. The proposal is based on the GTN model [21] accounting void nucleation as proposed by Chu and Needleman [30]. This section is aimed at summarizing such continuous model.

5.1. General overview of the GTN model

The yield function of the GTN model is given by

$$\phi(\boldsymbol{\sigma}, \bar{\varepsilon}, f) = \left(\frac{\sigma_e}{\bar{\sigma}}\right)^2 + 2q_1 f \cosh\left(-\frac{3}{2}q_2\frac{\sigma_m}{\bar{\sigma}}\right) - \left(1 + q_3 f^2\right) \tag{27}$$

being σ_e the von Mises stress, σ_m the hydrostatic pressure, q_β (with $\beta = 1, 2, 3$) material parameters to be calibrated, $\bar{\sigma} = \bar{\sigma}(\bar{\varepsilon})$ the yield stress of the fully dense matrix material ($f = 0$) which depends on the equivalent plastic strain, $\bar{\varepsilon}$, and f the material porosity which can reach a maximum value $f = 1/q_1$ for $\sigma_e = \sigma_m = 0$ and the widespread case of $q_3 = q_1^2$ [23,29].

The original version of Gurson model [12] was conceived to take into account the spherically symmetric deformation of a rigid perfectly plastic body which surrounds a spherical void. Then, Tvergaard [23,24] introduced the parameters q_1 and q_2 (also $q_3 = q_1^2$) as coefficients of the void volume fraction and hydrostatic pressure, respectively, for analyzing the case of uniaxial plane strain tension for elasto plastic materials with a periodic array of circular cylindrical voids. The adopted values of these parameters were $q_1 = 1.5$, $q_2 = 1.0$ and $q_3 = q_1^2 = 2.25$ instead of Gurson values which originally were $q_1 = q_2 = q_3 = 1$. The aforementioned parameters directly affect the material strength and post-elastic response of the material behavior. For example, the growth of q_1 increases the effect of the void volume fraction, resulting in a decrease of the material strength; q_2 accounts the effect of the hydrostatic stress into the inelastic material response: e.g., high values of q_2 lead to a strong softening response due to the void growth, revealing the annihilation of the strain hardening properties of the matrix material [31].

The internal parameters (q_β, with $\beta = 1, 2, 3, 4$) affect the failure behavior of the interface law proposed in this paper (described in Section 3) in the same way as above described: i.e., q_1 (and q_3) influences the effect of the void volume fraction, q_2 the effect of the normal contact stress while the new introduced constant q_4 allows to ponderate the effects of the tangential contact stress into the yield criterion. The influence of q_4 has been accurately reported and discussed in the numerical results section where a parametric study has been done.

The classical associated flow rule is employed for the continuous GTN model

$$\dot{\boldsymbol{\varepsilon}}^{\boldsymbol{p}} = \dot{\lambda}\frac{\partial \phi}{\partial \boldsymbol{\sigma}}. \tag{28}$$

The evolution of the void volume fraction is governed by

$$\dot{f} = (1 - f)\dot{\varepsilon}_{kk}^p + A(\bar{\varepsilon})\dot{\bar{\varepsilon}} \tag{29}$$

where the expression of A is given by Chu and Needleman [30] as

$$A = \frac{f_N}{s_N\sqrt{2\pi}} exp\left[-\frac{1}{2}\left(\frac{\bar{\varepsilon} - \varepsilon_N}{s_N}\right)^2\right] \tag{30}$$

being ε_N, s_N and f_N material parameters to be calibrated.

The microscopic equivalent plastic strain varies according to the equivalent plastic work balance [32]

$$(1 - f)\bar{\sigma}\ d\dot{\bar{\varepsilon}} = \boldsymbol{\sigma} : \ \mathbf{d}\boldsymbol{\varepsilon}^{\boldsymbol{p}}. \tag{31}$$

Finally, the hardening response is modeled through the following power law

$$\bar{\sigma} = \sigma_y \left(1 + \frac{E\bar{\varepsilon}}{\sigma_y}\right)^N = \sigma_y \left(1 + \frac{\bar{\varepsilon}}{\varepsilon_0}\right)^N \tag{32}$$

where σ_y is the initial matrix yield strength, E is the Young's modulus, N is the hardening exponent and ε_0 is the elastic limit.

5.2. Homogenization technique between GTN and interface model

It is noteworthy that in order to objectively compare the numerical simulations obtained by means of the discontinuous proposal, described in Section 2, with those results reached through the continuous GTN model of Section 5.1 a scale length need to be introduced (classically known as "characteristic length").

Particularly, the normal and tangential stiffness are calculated as

$$\mathbf{C} = \begin{pmatrix} \frac{E}{l} & 0 \\ 0 & \frac{G}{l} \end{pmatrix} \tag{33}$$

with E the Young's modulus, G the shear modulus and l the thickness of the joint.

The nucleation parameters of Eq. (12) are calculated as

$$u_N = \varepsilon_N l \tag{34}$$

$$s_{N_{IE}} = s_N l \tag{35}$$

with $s_{N_{IE}}$ the standard deviation of the nucleation law for the IE model and s_N the standard deviation for the corresponding continuous GTN model.

Finally, combining the power laws (15) and (32) with the relation $\varepsilon_0 = \frac{\sigma_y}{E}$ for the continuous elastic strain limit, the derived expression for the elastic strain limit of the discrete approach is obtained as follows

$$u_0 = \frac{\sigma_y l}{E}. \tag{36}$$

6. Numerical results

The numerical examples presented in this section are intended to demonstrate the basic features of the proposed interface model. With this purpose, a comparison between numerical simulations obtained through a well-established continuum proposal and results based on the discontinuous IE formulation are realized covering various material parameters and load conditions.

Numerical tests performed in failure Mode I, II and mixed are considered while the basic element patches, shown in Fig. 2, are employed. Particularly, the upper and bottom rigid elements are connected, in the first scheme (case of the continuous problem of Fig. 2a), through a 4-Node Plane Strain Isoparametric Element (4NPSIE) equipped with the non-linear GTN model. While, for the discontinuous analysis, a zero thickness IE connects such rigid elements (Fig. 2b). Therefore, the contact

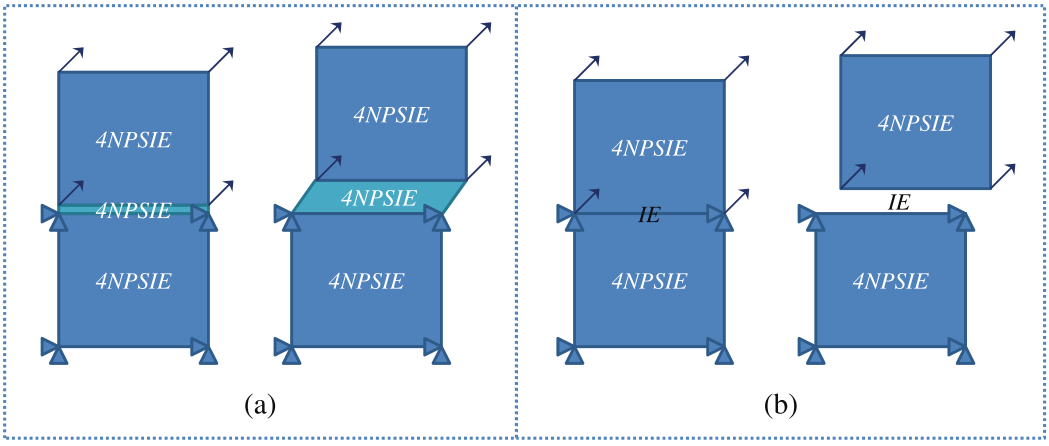

Fig. 2. Problem statement and boundary conditions: (a) continuous problem and (b) discontinuous approach based on the interface model.

interaction is modeled through the formulation proposed in Sections 2–4 which is implemented within the user-subroutine UINTER in Abaqus/Standard. For the numerical purpose, the upper and bottom rigid elements have unitary dimensions (1×1 cm^2) and displacement-based control is assumed.

In the first part of this section, a general comparison of the numerical responses obtained through the Continuous and the Discontinuous Model (CM and DM) is performed for a set of material parameters previously calibrated in a work of literature. Then, in the second and third part, the sensitivity of the model concerning the variation of different material parameters is tested and their influence on the final failure response for the three modes of failure is discussed.

6.1. Model prediction and comparison with the continuous-based model

In first place, stress histories activating failure processes under both Mode I, II and mixed types of fracture are investigated. Both normal and transverse relative displacements are co-imposed on the upper borders of the specimens, as highlighted in Fig. 2, while the remaining bottom borders are fixed with the aim of reproducing cracking processes under these three modes of fracture. Tensile displacements u are combined with transverse ones v defining a prefixed load angle θ (being $\tan\theta = u/v$).

In those analyses, the influence of the 4NPSIE thickness employed for the continuous-based simulations is comparatively evaluated against the same numerical tests obtained through the discrete crack approach. For this purpose, two different thicknesses $l = l_1 = 0.01$ mm and $l = l_2 = 0.1$ mm are considered into the numerical predictions (Fig. 3). All material parameters and variables are fixed while the thickness is modified in the continuous-based simulations. Based on typical values for steel grades, calibrated for the model identification in previous works available in literature [21], the following GTN model parameters are herein assumed: $q_1 = 1.5$, $q_2 = 1$ and $q_3 = q_1^2 = 2.25$; the nucleation parameters $\varepsilon_N = 0.3$, $s_N = 0.08$, $f_N = 0.5$ and $f_0 = 0.005$; the Young's modulus $E = 210$ GPa and the Poisson's coefficient $\nu = 0.3$; and finally, according to the power hardening law of Eq. (32) the exponent $N = 0.1$ and the yield strength $\sigma_y = 300$ MPa are used. However, the model testing through the parametric study implies a variation of all of them. The model parameters for the IE problem are calculated as explained in Section 5.2. Then, the adopted value for q_4 is assumed equal to 3 as justified in the following subsections.

The numerical results for the first 4NPSIE thickness $l_1 = 0.01$ mm and the respective results from the interface constitutive formulation are firstly presented and discussed. Failure Mode I results can be seen in Fig. 4. On the left (Fig. 4a) the results in terms of normal stress vs. opening displacement u are presented for both approaches. The comparison between them demonstrates that the peak values in both formulations are reached for the same displacement level, showing a very small difference in terms of peak stress. As a result of the simulations the results based on the continuous GTN model highlight a small major strength compared with that of the porous-based interface modeling. Beside the peak value, the softening slope of the curve is slightly more pronounced for the continuous approach, due to the faster increase of the porosity as clearly figures out on the right side of Fig. 4b where the internal porosity evolution and the subsequent nucleation of new voids and growth of the existing ones are described during the whole fracture processes.

The numerical simulations obtained under failure Mode II are presented in Fig. 5. The results in terms of shear stress vs. lateral displacement (Fig. 5a) show an almost perfect agreement between the compared approaches. Furthermore, Fig. 5b reports the corresponding evolution of the total porosities for both GTN model and IE-based proposal. It is worth highlighting that f_{gro}, meaning the evolution due to the growth of existing voids, is null under shear load cases while the initial void fraction is $f_0 = 0.005$. Due to these reasons and for the sake of clarity, only the total void volume fraction f is plotted in Fig. 5b, since f_{nuc} and f are parallel and nearly coincident. As occurs with the case of direct tensile stress, an excellent concordance

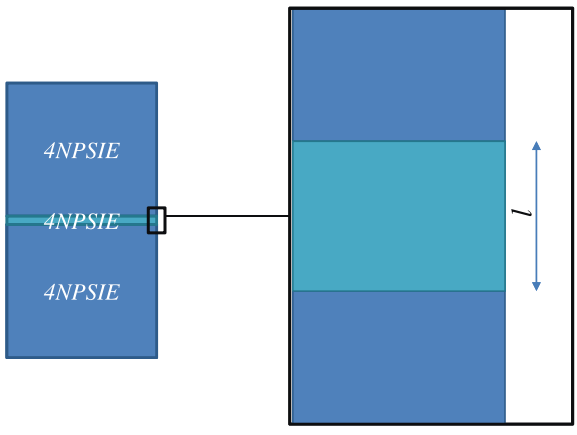

Fig. 3. Thickness detail l of the 4-node isoparametric elements analyzed in the ductile fracture simulations.

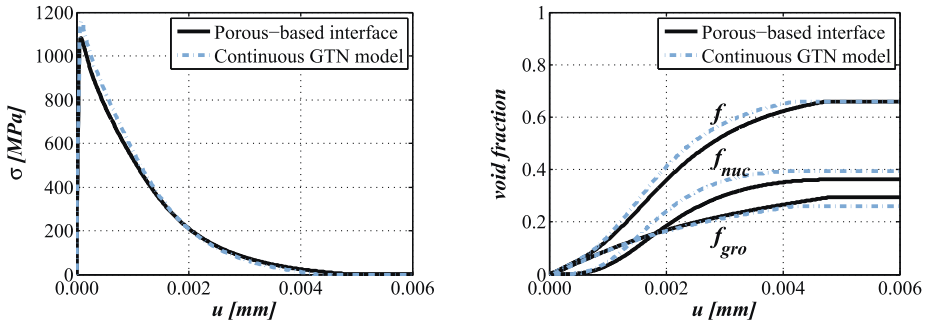

(a) Tensile stress vs. normal displacement (b) Void volume fraction vs. normal displacement

Fig. 4. Continuous vs. discontinuous simulation of tensile tests with $l_1 = 0.01$ mm.

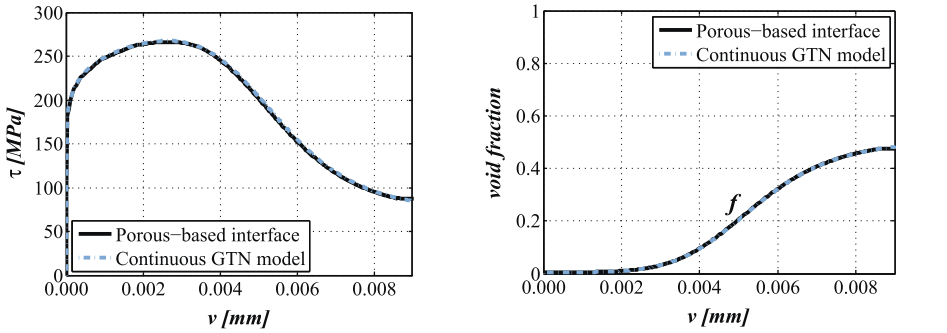

(a) Shear stress vs. transverse displacement (b) Void fraction vs. transverse displacement

Fig. 5. Continuous vs. discontinuous simulation of shear tests with $l_1 = 0.01$ mm.

can also be seen between the models under failure Mode II. The proposed tests deal with a shear-hardening response in the first part of the simulation, then, once the total porosity reaches the value $f = 0.020$ a shear-softening behavior characterizes the failure Mode II response of the considered analysis.

Beside the performed Mode I and II, the results for a mixed Mode of failure are now discussed. For the sake of brevity, the only case in which $\theta = 45^\circ$ is analyzed. Numerical analyses show on the one hand, the very good agreement between the CM and DM on the numerical predictions when normal stress vs. opening displacement curves (Fig. 6a) are compared. On the other hand, the results in terms of tangent stress vs. transverse displacement illustrate the same kind of post-elastic behavior. Particularly, after the peak a sharp loss of strength takes place at which follows an hardening response with a final softening behavior. Even the response is quite similar analyzing both approaches, a significant difference in shear strength characterizes both simulations. In spite of the agreement is not so good for the shear side, it is worth noting that the order of magnitude is much lower when compared to the normal stresses. Based on this, a small effect on the structural behavior of the whole mixed mode process can be observed. Particularly, Fig. 7 reports the total reaction, F_{TOT}, vs. the total mixed mode displacement, u_{TOT}, where

$$F_{TOT} = \sqrt{F_N^2 + F_T^2} \tag{37a}$$

$$u_{TOT} = \sqrt{u^2 + v^2} \tag{37b}$$

being F_N and F_T the resulting reactions in the normal and shear directions, respectively; while u and v are the normal and shear displacements.

Moreover, a second 4NPSIE thickness $l_2 = 0.1$ mm is considered and the same failure cases as before, for l_1, are analyzed. Particularly, the numerical results of the first load case, corresponding to failure Mode I, are illustrated in Fig. 8. Then, Fig. 9 reports the shear–displacement curves of failure Mode II and finally, Fig. 10 highlights the mixed mode of fracture considering the 45° load condition.

Almost the same observations can be stated for these second family of tests. The behavior in Mode I is analogous to that of the previous case in terms of stress and porosity evolutions as well. Then, the agreement in Mode II is excellent, while the same conclusions made for the first 4NPSIE thickness test loaded in mixed mode can be observed (i.e., there is a considerable difference when the shear stress vs. transverse displacement curves of the two models are compared, however this does not affect significantly the overall response of the mixed mode of failure). It is worth highlighting that Figs. 4–10 demonstrate a

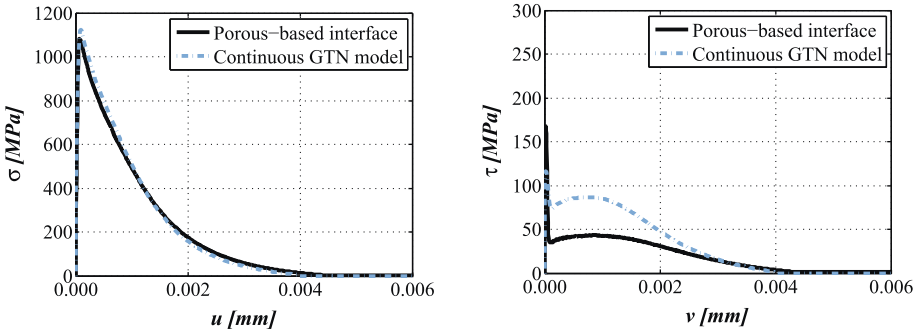

(a) Tensile stress vs. normal displacement (b) Shear stress vs. transverse displacement

Fig. 6. Continuous vs. discontinuous simulations of mixed mode tests for $\theta = 45^\circ$ with $l_1 = 0.01$ mm.

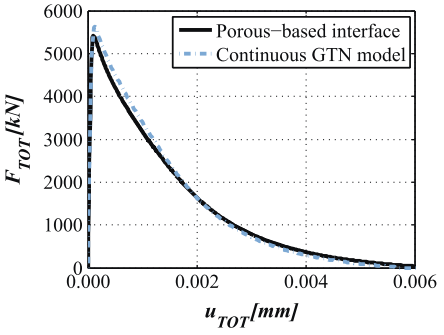

Fig. 7. Total force vs. total displacement for $\theta = 45^\circ$ with $l_1 = 0.01$ mm.

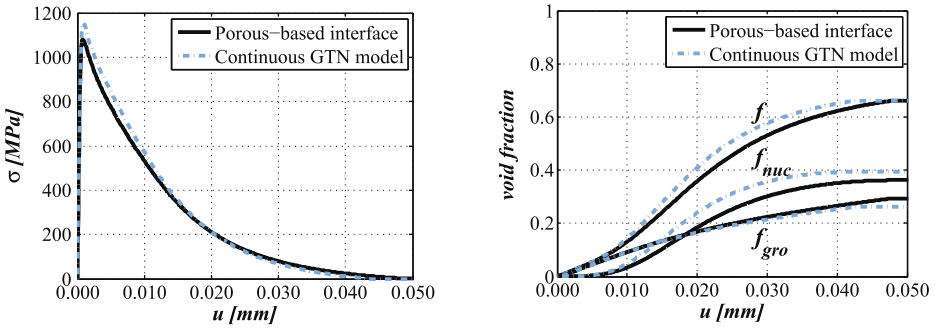

(a) Tensile stress vs. normal displacement (b) Void volume fraction vs. normal displacement

Fig. 8. Continuous vs. discontinuous simulation of tensile tests with $l_2 = 0.1$ mm.

rather good agreement between both models when the same set of input parameters are considered for describing the elastic and failure response of the ductile fracture process.

Finally, in Fig. 11a and b a comparison of the normal and shear stresses against normalized uplift/transverse displacements is illustrated. Particularly, Fig. 11a summarizes the results of Figs. 4a and 8a, as well as Fig. 11b does the same with Figs. 5a and 9a. All results are unified through normalizing the normal/shear displacements with the corresponding 4NPSIE thickness (labeled l_1 and l_2). A perfect agreement can be observed for both 4NPSIE thicknesses employing the two aforementioned models, even more keeping in mind that the same set of material parameters are used in all simulations.

6.2. Parametric sensitivity analysis of material parameters

In this subsection $\theta = 45^\circ$ fracture mixed mode cases, as shown in Fig. 2, are considered. The adopted material parameters for the CM are summarized in Table 1 and, consequently, for the IE problem are derived as explained in Section 5.2.

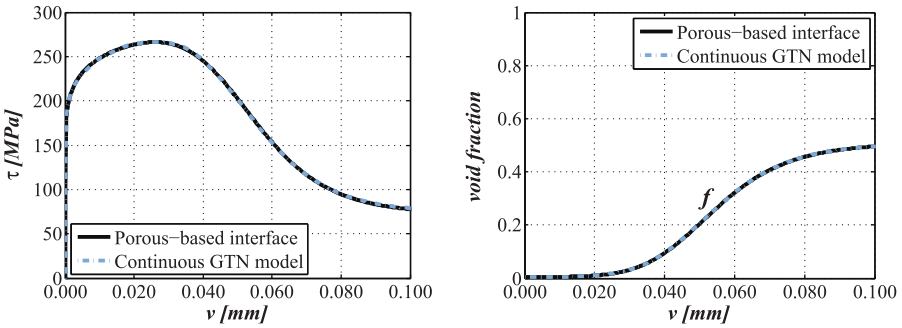

(a) Shear stress vs. transverse displacement (b) Void volume fraction vs. transverse displacement

Fig. 9. Continuous vs. discontinuous simulation of shear tests with $l_2 = 0.1$ mm.

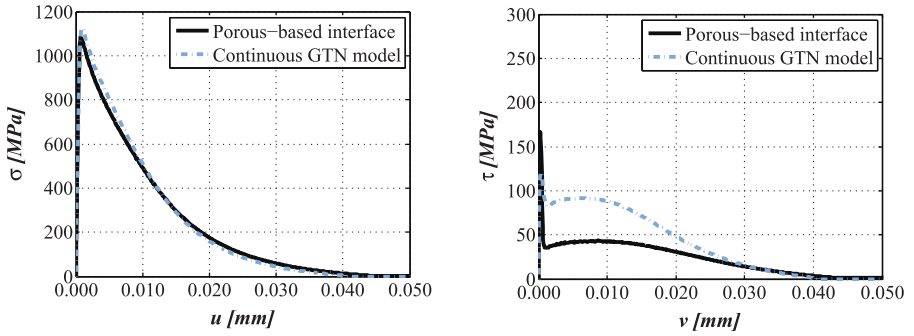

(a) Tensile stress vs. normal displacement (b) Shear stress vs. transverse displacement

Fig. 10. Continuous vs. discontinuous simulation of mixed mode tests for $\theta = 45^\circ$ with $l_2 = 0.1$ mm.

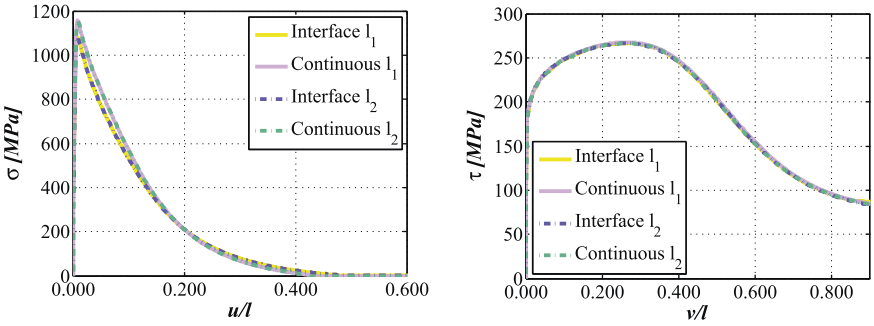

(a) Tensile stress vs. normalized Mode I displacement (b) Shear stress vs. normalized transverse displacement

Fig. 11. Stresses vs. normalized displacements for both $l = l_1$ and $l = l_2$.

Furthermore, the q_i parameters are: $q_1 = 1.5$, $q_2 = 1$ and $q_3 = 2.25$ in both the CM and the DM, while for the six IE cases $q_4 = 3$. The influence of the last one is addressed more widely in subSection 6.3.

The main purpose of these analyses is to evaluate the capability of the proposed IE to predict failure behavior of metal joints under general mixed modes of fracture when a series of internal parameters are considered. The study is focused on the sensitivity analysis of the model parameters involved in the simulation. The comparison between these numerical results with those obtainable with a well-established GTN model are shown.

As a starting point, a reference test is considered and labeled as C1 case. Beside this, the initial porosity, the nucleation parameters, the yield strength, the hardening exponent of the hardening rule, are modified one at a time with the aim of consider several cases (from C2 to C6 cases) as figures out in Table 1.

Table 1
Material parameters for the continuous model.

Case	σ_y (MPa)	Hard. exp.	f_0	ε_N	f_N	s_N
C1	300	0.10	0.005	0.3	0.5	–[a]
C2	300	0.10	0.005	0.3	1.0	
C3	300	0.10	0.050	0.3	1.0	0.08
C4	300	0.10	0.050	0.2	1.0	
C5	300	0.15	0.050	0.2	1.0	
C6	200	0.10	0.050	0.2	1.0	

[a] Test of reference.

Fig. 12 highlights the total reactions, F_{TOT}, vs. the total mixed mode displacements, u_{TOT} for the analyzed *Ci* cases. These results demonstrate the phenomenological capabilities of the interface model to reproduce failure processes of ductile fracture in metals, when it is applied a discontinuous-based FE modeling. As a matter of result, the numerical predictions based on the IE analyses compared against the same results, employing a largely validated GTN model, demonstrate a very good agreement for each considered case. Furthermore, no special influence on the accuracy of the proposed model can be observed due to the variation of any of the model parameters.

6.3. Parametric sensitivity analysis: influence of q_4

The third numerical examples involve a direct shear test under different values of the q_4 parameter. This latter represents the only additional parameter introduced in the zero-thickness interface formulation. As it can be inferred from Eq. (7), it affects the failure Mode II response and, consequently, the mixed one. In other words, the proposed failure criterion for the IE proposal is not affected by q_4 when the pure tensile case is considered.

As described above, the Mode II of failure in this work is accomplished by progressively applying a relative shear displacement to the nodes on the top surface whereas the nodes situated at the bottom one remain fixed (Fig. 2). The parameters used for this example for the CM are: $q_1 = 1.5,\ q_2 = 1,\ q_3 = q_1^2 = 2.25,\ \varepsilon_N = 0.3,\ s_N = 0.08,\ \ f_N = 0.5,\ f_0 = 0.005,$ $E = 210$ GPa, $v = 0.3$, $\sigma_y = 300$ MPa and $N = 0.1$.

Shear traction and the total void volume fraction evolution against the relative tangential displacement are plotted for different values of q_4 ($q_4 = 1, 2, 3$ and 4) in Fig. 13. The Mode II results demonstrate the influence of this parameter on the shear capacity of the interface. A decreasing shear strength can be registered as q_4 increases. After the peak, all curves show a similar post-peak behavior characterized by a steeper softening response when $q_4 = 1$ compared with that obtained for higher values of such parameter.

A perfect agreement between the responses based on the continuous against the proposed IE-based model is reached for a value of $q_4 = 3$, which is used for the totality of the numerical examples in this work. A lower value leads to an overestimation of the shear strength of the contact, while, on the contrary, a higher value conduce to underestimate the Mode II of resistance.

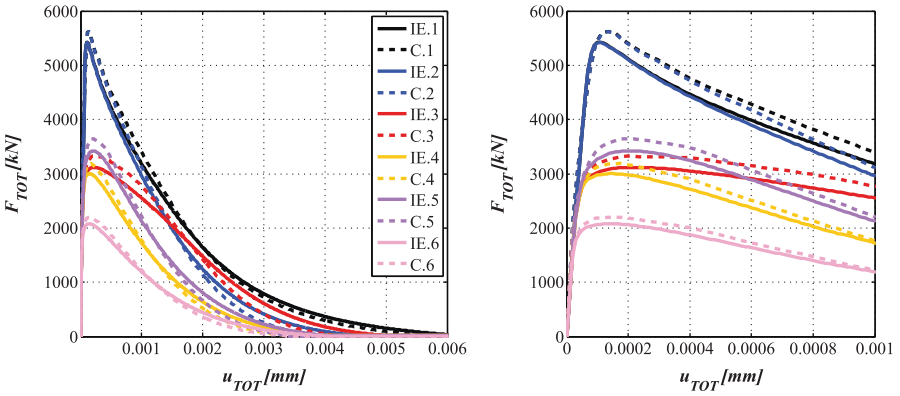

(a) Plot range considering displacements up to failure.

(b) Detail of the peak zone.

Fig. 12. Continuous vs. discontinuous simulation of mixed mode tests for $\theta = 45^\circ$ for various material parameters.

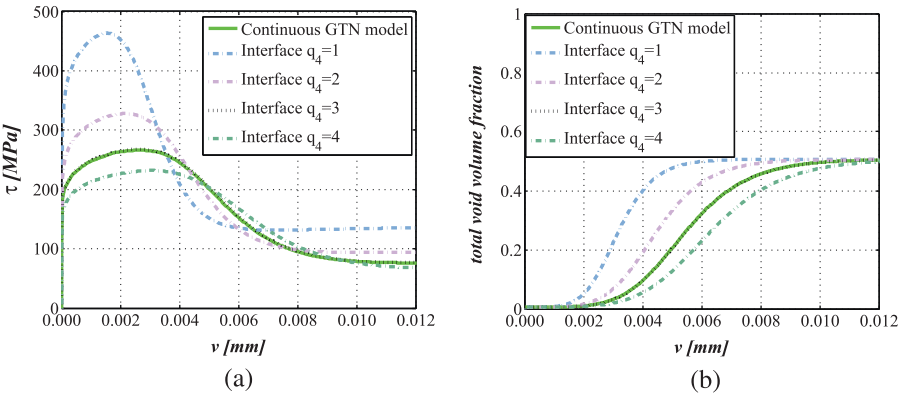

Fig. 13. Influence of q_4: (a) τ–v and (b) total void volume fraction-v curves.

7. Conclusions

In the context of ductile fracture modeling, a new zero-thickness interface element conceived within the general framework of fracture mechanics and porous plasticity has been presented in this paper. A series of final remarks can be drawn out on the bases of both the model formulation and the proposed applications:

- Although a large amount of models derived from the original Gurson model exist, the authors have no knowledge of any discontinuous proposal based on the direct extension of this class of formulation. The model proposed in this work actually represents a key novelty in this aspect.
- The numerical results obtained through the proposed interface formulation show an excellent agreement with those obtained with the well-established continuous-based GTN model, which has largely been validated in scientific literature and represents, as a matter of fact, one of the main pillars in the field of ductile fracture modeling in metals.
- There is a proportional correspondence between the parameters of the continuous approach with those of the discontinuous model, making all the available research on material parameters directly applicable.
- Only one additional parameter, q_4, has to be adjusted in order to keep similar post-elastic responses employing the aforementioned models. In the whole comparisons, realized during the model testing, q_4 assumed values within the range 2.5–3. Particularly, the value adopted in this work is $q_4 = 3$.

Further validations of the proposed interface formulation in structural scale cases as well as its extension in transient thermomechanical problems represent, among others, future steps of this research line. The interface model proposed in this paper could also be employed in mesoscopic analyses aimed at simulating failure processes possibly developing at interfaces of second phase particles and inclusions.

Acknowledgements

The support of INTI (Instituto Nacional de Tecnología Industrial, Argentina) and Roberto Rocca Education Program, through their respective grants, is gratefully acknowledged by D.S.S.

References

[1] Horstemeyer MF, Gokhale AM. A void-crack nucleation model for ductile metals. Int J Solids Struct 1999;36(33):5029–55.
[2] Kim J, Gao X, Srivatsan T. Modeling of crack growth in ductile solids: a three-dimensional analysis. Int J Solids Struct 2003;40(26):7357–74.
[3] Tvergaard V, Hutchinson JW. Two mechanisms of ductile fracture: void by void growth versus multiple void interaction. Int J Solids Struct 2002;39(13):35813597.
[4] Nielsen KL, Tvergaard V. Failure by void coalescence in metallic materials containing primary and secondary voids subject to intense shearing. Int J Solids Struct 2011;48(9):1255–67.
[5] Barsoum I, Faleskog J. Rupture mechanisms in combined tension and shear-experiments. Int J Solids Struct 2007;44(6):1768–86.
[6] Barsoum I, Faleskog J. Rupture mechanisms in combined tension and shear-micromechanics. Int J Solids Struct 2007;44(17):5481–98.
[7] Barsoum I, Faleskog J. Micromechanical analysis on the influence of the Lode parameter on void growth and coalescence. Int J Solids Struct 2011;48(6):925–38.
[8] Bonora N, Gentile D, Pirondi A, Newaz G. Ductile damage evolution under triaxial state of stress: theory and experiments. Int J Plast 2005;21(5):981–1007.
[9] Benzerga A, Surovik D, Keralavarma S. On the path-dependence of the fracture locus in ductile materials – analysis. Int J Plast 2012;37(0):157–70.
[10] Jin C, Niu J, He S, Fu C. Modeling thermal cycling induced micro-damage in aluminum welds: an extension of Gurson void nucleation model. Comput Mater Sci 2008;43(4):1165–71.
[11] Crété J, Longére P, Cadou J. Numerical modelling of crack propagation in ductile materials combining the GTN model and X-FEM. Comput Methods Appl Mech Eng 2014;275:204–33.

[12] Gurson AL. Continuum theory of ductile rupture by void nucleation and growth: Part I – Yield criteria and flow rules for porous ductile media. J Eng Mater Technol 1977;99(1):2–15.
[13] Enakoutsa K. An improved nonlocal Gurson model for plastic porous solids, with an application to the simulation of ductile rupture tests. Appl Math Model 2014;38:2791–9.
[14] Dormieux L, Kondo D. An extension of Gurson model incorporating interface stresses effects. Int J Eng Sci 2010;48(6):575–81.
[15] Jackiewicz J. Use of a modified Gurson model approach for the simulation of ductile fracture by growth and coalescence of microvoids under low, medium and high stress triaxiality loadings. Eng Fract Mech 2011;78(3):487–502.
[16] Nahshon K, Xue Z. A modified Gurson model and its application to punch-out experiments. Eng Fract Mech 2009;76(8):997–1009.
[17] Nahshon K, Hutchinson J. Modification of the Gurson model for shear failure. Eur J Mech – A/Solids 2008;27(1):1–17.
[18] Zhang Z, Thaulow C, Odegard J. A complete Gurson model approach for ductile fracture. Eng Fract Mech 2000;67(2):155–68.
[19] Nielsen KL, Tvergaard V. Ductile shear failure or plug failure of spot welds modelled by modified Gurson model. Eng Fract Mech 2010;77(7):1031–47.
[20] Benallal A, Desmorat R, Fournage M. An assessment of the role of the third stress invariant in the Gurson approach for ductile fracture. Eur J Mech – A/Solids 2014;47(0):400–14.
[21] Tvergaard V, Needleman A. Analysis of the cup-cone fracture in a round tensile bar. Acta Metall 1984;32(1):157–69.
[22] Savalia P, Tippur H, Kirugulige M. A numerical study of inclusion–matrix debonding in the presence of a nearby crack. Eng Fract Mech 2008;75(5):926–42.
[23] Tvergaard V. Influence of voids on shear band instabilities under plane strain conditions. Int J Fract 1981;17(4):389–407.
[24] Tvergaard V. On localization in ductile materials containing spherical voids. Int J Fract 1982;18(4):237–52.
[25] Tvergaard V. Effect of pure mode I, II or III loading or mode mixity on crack growth in a homogeneous solid. Int J Solids Struct 2010;47(11–12):1611–7.
[26] Caggiano A, Etse G, Martinelli E. Zero-thickness interface model formulation for failure behavior of fiber-reinforced cementitious composites. Comput Struct 2012;98–99:23–32.
[27] Caggiano A, Said Schicchi D. A thermo-mechanical interface model for simulating the bond behaviour of FRP strips glued to concrete substrates exposed to elevated temperature. Eng Struct 2015;83:243–51.
[28] Sánchez P, Huespe A, Anca A, Sonzogni V. Modos de falla dúctil y bifurcación material utilizando el modelo constitutivo de Gurson. Mecánica Comput 2006;25:1975–95.
[29] Abaqus, Abaqus Documentation Dassault Systémes, Providence, RI, USA; 2012.
[30] Chu C, Needleman A. Void nucleation effects in biaxially stretched sheets. J Eng Mater Technol 1980;102(3):249–56.
[31] Kossakowski P. The analysis of influence of Tvergaard's parameters on S235JR steel response in high stress triaxiality. Adv Mater Sci 2012;12(1):27–35.
[32] Aravas N. On the numerical integration of a class of pressure-dependent plasticity models. Int J Numer Methods Eng 1987;24:1395–416.